iMPACT: An Innovative Tracker and Calorimeter for Proton Computed Tomography

Serena Mattiazzo, Filippo Baruffaldi, Dario Bisello, Benedetto Di Ruzza, Piero Giubilato, Roberto Iuppa, Chiara La Tessa, Devis Pantano, Nicola Pozzobon, Ester Ricci, Walter Snoeys, and Jeffery Wyss

***Abstract*—This contribution describes the first results obtained within the iMPACT project, which aims to build a novel proton computed-tomography (pCT) scanner for protons of energy up to 230 MeV, as used in hadron therapy. The iMPACT pCT scanner will improve the current state-of-the-art in proton tracking at all levels: speed, spatial resolution, material budget, and cost. We will first describe the design of the iMPACT scanner, which is composed by a tracker and a range calorimeter. We will then illustrate the results of a test with the ALPIDE sensor, a monolithic active pixels sensor, developed by the ALICE collaboration, which will equip the iMPACT tracker in this first phase. We finally detail the characterization building elements of the prototype of the range calorimeter, which is composed of segmented scintillator fingers readout by SiPMs. Reported beam-test data will highlight how the technological choices we made well address the performances of a state-of-the-art pCT system.**

***Index Terms*—Biomedical imaging, particle tracking, silicon radiation detectors.**

I. Introduction

IN RECENT years the use of energetic protons and carbon ions (hadrons) for cancer radiation treatment has grown in importance among all major industrialized nations. The most recent studies report how radiation treatment using protons (^{1}H) and carbon ions (^{12}C) leads to improvements in treatment of many cancer types [1]. Modern superconducting cyclotrons are compact machines and make possible the acceleration of protons up to 250 MeV/u and ^{12}C ions up to about 500 MeV/u, enabling the practical realization of hadron therapy facilities worldwide [2]. Hadron therapy is in the process of joining the already established X-ray therapy as an effective radiation therapy to treat cancer disease. The effectiveness of proton treatment is however, currently limited by the necessity to rely on X-rays CT data to plan the dose delivery, which worsens the intrinsic precision that hadron therapy could achieve [3]. Indeed many groups are investigating the way to realize a proton CT which would overcome the aiming limitation by using protons instead of photons to image the target tissue density [4], [5]. In addition, the dose delivered to the patient with a proton computed-tomography (pCT) is limited to few mGy, at least an order of magnitude lower than the dose delivered with a traditional X-ray CT (10–100 mGy) [6], [7].

Manuscript received January 25, 2018; revised March 19, 2018; accepted April 6, 2018. Date of publication April 11, 2018; date of current version July 2, 2018. This work was supported by the European Research Council through the European Union's Horizon 2020 Research and Innovation Program under Grant 649031. *(Corresponding author: Serena Mattiazzo.)*

S. Mattiazzo, D. Bisello, P. Giubilato, D. Pantano, and N. Pozzobon are with the Department of Physics and Astronomy, University of Padova, 35131 Padua, Italy, and also with the Istituto Nazionale di Fisica Nucleare, Trento Institute for Fundamental Physics and Applications, Conseil Européen pour la Recherche Nucléaire, 35131 Padua, Italy (e-mail: serena.mattiazzo@pd.infn.it; bisello@pd.infn.it; giubilato@pd.infn.it; dpantano@pd.infn.it; nicola.pozzobon@pd.infn.it).

F. Baruffaldi is with the Department of Physics and Astronomy, University of Padova, 35131 Padua, Italy (e-mail: filippo.baruffaldi@studenti.unipd.it).

B. Di Ruzza is with the Department of Electrical Engineering and Information Technology, Politecnico di Bari, 70125 Bari, Italy (e-mail: benedetto.diruzza@gmail.com).

R. Iuppa, C. La Tessa, and E. Ricci are with the Department of Physics, University of Trento, 38123 Trento, Italy, and also with the Trento Institute for Fundamental Physics and Applications, 38123 Trento, Italy (e-mail: roberto.iuppa@unitn.it; chiara.latessa@tifpa.infn.it; ester.ricci@unitn.it).

W. Snoeys is with CERN, 1210 Geneva, Switzerland (e-mail: walter.snoeys@cern.ch).

J. Wyss is with the DICeM, University of Cassino and Lazio Meridionale, 03043 Cassino, Italy, and also with INFN Padova, 50019 Padua, Italy (e-mail: wyss@unicas.it).

Color versions of one or more of the figures in this paper are available online at http://ieeexplore.ieee.org.

Digital Object Identifier 10.1109/TRPMS.2018.2825499

II. Proton Computed Tomography

One of the drawbacks of pCT, when compared to a standard X-ray CT, is that protons undergo multiple-Coulomb scattering as they move through matter. This affects the image spatial resolution (limited to ∼5 mm as long as a standard tomography approach is employed [8]), blurring the resulting 3-D reconstructed image. This effect can be overcome by adding the knowledge of each individual proton trajectory. However, the real path of a proton inside the body is unknown, and some type of estimation is therefore required to achieve an optimal pCT imaging. One of the most promising approaches is to infer the proton most likely path by measuring its entry and exit vectors (angle and position) together with the energy it lost in the target. With this technique, a spatial resolution of 1 mm can be achieved [8], [9], while, for comparison, an X-ray CT provides a spatial resolution of ∼500 μm [10]. A device designed to retrieve such parameters for each proton traversing the target is called scanner.

A pCT scanner is therefore usually composed by two tracking stations, one before and one after the patient, to measure the proton entry and exit trajectories, and by a calorimeter, to measure the residual proton energy.

The number of required proton tracks to reconstruct a 3-D image with the necessary resolution (spatial resolution better than 1 mm, energy resolution better than 1%) has been

estimated in [11]: in a volume of $10 \times 10 \times 10$ cm^3, about 10^9 tracks have to be measured.

Present state-of-the-art pCT prototypes made excellent advancements in the field, but they still show some limitations for a practical implementation. The custom-made technologies typically used (micro-strips [12], [13], scintillating fibers [14], and gas detectors [15]) limit their convenient application in commercial systems or they are undesirable in a hospital environment (due to the use of detectors and/or high voltages). In addition, the above-mentioned pCT prototypes are limited in terms of data acquisition speed, so that they all require exposure times of the order of many minutes, too long for a practical implementation of the technique [4] due to the inevitable movements of the patient (breathing) and discomfort over such long period. Data processing time is another important issue: depending on the optimization of the reconstruction code, as well as the level of parallelization (i.e., the number of CPUs and GPUs used), two billions proton tracks can be reconstructed in less than 10 min [16], [17].

III. iMPACT Design

A. Overview

The goal of the iMPACT project is to build a proton scanner able to collect more than 10^9 proton tracks in 10 s, possibly less, and to use only commercially available solutions, in order to keep the system simple and to reduce costs.

Recording 10^9 protons in 10 s means being able to sustain a 100 MHz global rate. Considering a reference irradiation area of about 100 cm^2, this is equivalent to a 1 MHz cm^{-2} rate. This is the minimal baseline goal of the project, even if the design actually aims at a factor 10 faster system.

The planned solution of iMPACT presents several novel aspects: the tracker will use matrices of monolithic pixel detectors and a highly segmented range calorimeter will measure the proton residual energy [18], [19]. In the next two sections, a detailed description of the two detectors is given.

IV. iMPACT Tracker

A. Introduction

The guidelines for the tracker are to develop a fast sensor, capable of handling a particle flux of 1 MHz cm^{-2}, with a low material budget to minimize multiple scattering of the protons. The sensor will be realized with commercially available CMOS processes, to reduce costs and ensure scalability. To simplify development and commissioning, the tracker will be organized as a modular composition of independent sensors.

To fulfill the requirements of a real clinical medical application, the active surface must exceed 10×10 cm^2. The final sensor should therefore be as large as possible to minimize dead areas and reduce the material budget, by avoiding any support structure along the beam path. Sensors exploiting full reticules sizes of about 5 cm^2 are already possible and, by stitching, the area of the single sensor might be increased up to 10–15 cm^2 [20]. By clustering all the electronics off to the sensor periphery and tiling several sensors, it will be possible to cover the large area required in the real application.

Fig. 1. ALPIDE sensor on the carrier board.

B. Sensor for the IMPACT Tracker

To realize the tracker sensor, the iMPACT team is collaborating with the ALICE experiment at CERN. The starting point is the ALPIDE chip [21], a monolithic active pixels sensor (MAPS), built in a 180 nm CMOS imaging process, that the ALICE collaboration has developed for the upgrade of the inner tracking system (Fig. 1).

ALPIDE is fabricated on a high-resistivity (higher than 1 kΩ·cm) 25 μm thick epitaxial layer, grown on a p-type substrate. A reverse bias voltage (up to $V_{\text{substrate}} = -6$ V) can be applied to the substrate to increases the depletion volume around the *n*-well collection diodes and reduce their capacitance. Both effects increase the signal to noise ratio. A depleted substrate also ensures a fast charge collection by drift and reduces the cluster size (which reduces the amount of data at the chip output). The sensitive matrix contains 512×1024 pixels with 28 μm pitch, for a total active area of 2.9 cm $\times$ 1.4 cm (full reticule size), with in-pixel amplification, shaping, discrimination, and multievent buffering. The matrix readout is hit driven, i.e., there is no signaling activity over the matrix if there are no hits to read out. Analog power consumption in the ALPIDE matrix is about 5 mW/cm^2, almost independent on the hit rate, while the digital power consumption in the matrix is below 1 mW/cm^2 for a hit rate of 100 kHz/cm^2. Primarily due to the transmitter in the periphery, the power consumption of the full chip is much higher (<40 mW/cm^2). The readout of the data frame from the matrix is zero-suppressed: only the addresses of pixels actually hit are sent off chip, thus limiting the data output. The chip has been thinned to 50 μm to minimize material budget, hence proton scattering.

While a pixel pitch of 28 μm provides a better tracking resolution with respect to present trackers based on strip, this is not expected to actually improve the final spatial resolution. As a matter of fact, the image reconstruction precision is intrinsically limited by the particle scattering inside the target. A smaller pitch allows to handle a higher particle rate.

C. Planned Tracker Layout

The ALPIDE sensor is the largest chip available with the required features (a depleted and fast MAPS), even though does not have the ideal size for the final tracker. In order to cover an area of tens of cm^2 with several ALPIDE chips, a support structure is necessary. We will exploit a modified version

Fig. 2. Photograph of one IB stave (seen from the carbon spaceframe).

of the "staves" (the building block of the detector) used for the inner barrel (IB) of the ALICE tracker (Fig. 2). Each IB stave is instrumented with nine pixel chips in a row, hence covering a total active area of 15 mm $\times$ 270 mm. The gap between adjacent chips is about 100 μm. The chips are connected via laser soldering to a copper flexible printed circuit (FPC), which takes data out of the module (electronics is not clustered on one side of the chip). The mechanical support (spaceframe) is in carbon. The FPC and the spaceframe contribute to the material budget with a silicon equivalent thickness of about 50 μm each: the total material budget of each plane will about 150 μm of silicon, including the ALPIDE chip. Five staves will be finally aligned in the vertical direction. The total area of one plane will be therefore 27 cm $\times$ 7.5 cm.

D. Test Beam Results

The ALPIDE sensor has been widely tested with minimum ionizing particles [21] but never with protons in the hadron therapy energy range (<230 MeV). The sensor was therefore tested in July 2017 at TIFPA beam line hosted at the APSS Proton Therapy Centre (Trento, Italy) [22]. The irradiation facility is fed by an IBA Proteus 235 cyclotron which can deliver protons with energies between 70 MeV and 228 MeV. Outside clinical hours, the beam can be redirected toward the experimental room, where the beam energy can be further lowered down to 15 MeV by using calibrated degraders. The beam size and maximum particle rate ranges, according to the energy, from a size of 6.8 mm (FWHM) and a maximum particle rate of $2.3 \cdot 10^8$ p/sec at 228 MeV, to 16.2 mm (FWHM) and a maximum flux of $3.8 \cdot 10^6$ p/sec at 70 MeV. Beam intensity values here reported correspond to 1 nA beam current requested at beam extraction. The beam extraction current varied in the range 1–300 nA. If necessary, low particle rates of the order of 10^2 Hz can be obtained at the isocenter (the beam focus position).

The particle rate has been set to about 5 kHz on the scintillator during our test. Since the beam profile is Gaussian, with an FWHM of about 1 cm (see Fig. 4), the particle rate can be estimated to be in the order of few kHz/cm^2. The number of active pixels per proton (cluster size) in the ALPIDE sensor was studied at different proton beam energies and with different backside voltages applied to the substrate. Fig. 3 shows the change of the cluster size with proton energy for $V_{\text{substrate}}$ ranging from 0 to -6 V.

The cluster size decreases when proton energy increases and also with backside voltage (in absolute value); this has a significant impact on the tracker data throughput. For $V_{\text{substrate}} = 0$ V, the average number of pixels for each cluster goes from 12 at 15 MeV, down by a factor 3 to just 4 pixels per cluster at 228 MeV. The cluster size shrinks at a higher bias voltage: at $V_{\text{substrate}} = -3$ V the cluster size varies from an average of

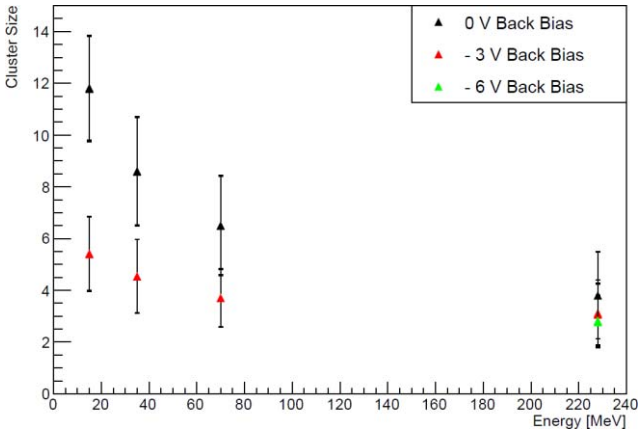

Fig. 3. Evolution of the cluster size as a function of the proton energy. The errors bars are the RMS of the cluster size distributions for each run.

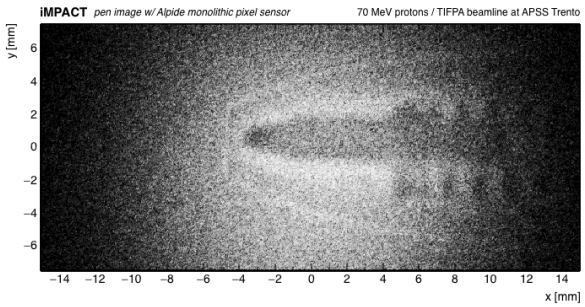

Fig. 4. Proton radiography of a pen with the ALPIDE sensor, taken during the TIFPA test beam.

3 pixels at 228 MeV to 5 at 15 MeV. At $V_{\text{substrate}} = -6$ V and at the maximum beam energy, the cluster size shows a further slight decrease; no data are available for this bias value at lower energies. The foundry also provides a process modification to fully deplete the epitaxial layer, which has been implemented in a previous ALPIDE version [23] and which would further reduce the cluster size.

Fig. 4 shows a quick demonstrative radiography of a plastic ball pen with the ALPIDE sensor and 70 MeV protons performed at the spur of the moment: it clearly illustrates the potential of large area MAPS sensors in imaging applications. Proton counts per pixel are shown in a gray scale, which is not linear for enhanced clarity of the picture. The distance between the pen and the ALPIDE sensor was about 2 cm. Material with different densities can be distinguished: the plastic tip, the iron spring, the ink straw, and the steel ballpoint (the densest and consequently the darkest part).

V. iMPACT Calorimeter

A. Design of the iMPACT Calorimeter

The iMPACT pCT scanner employs a fast achromatic segmented scintillator calorimeter to measure the protons energy after they passed through the target. The calorimeter is achromatic as it derives the particle energy by directly measuring the path length (range) in an absorber of known characteristics rather than measuring the deposited energy, like in traditional setups. To do so, the scintillator calorimeter is segmented into

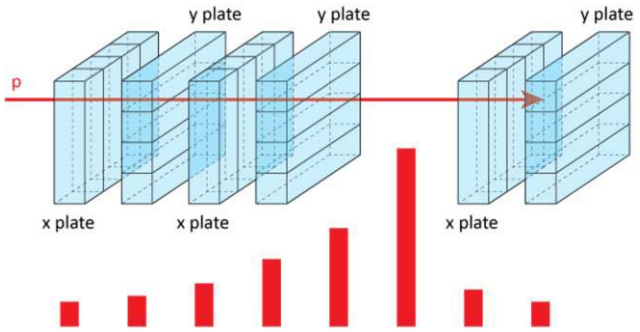

Fig. 5. Layout of the proposed range calorimeter.

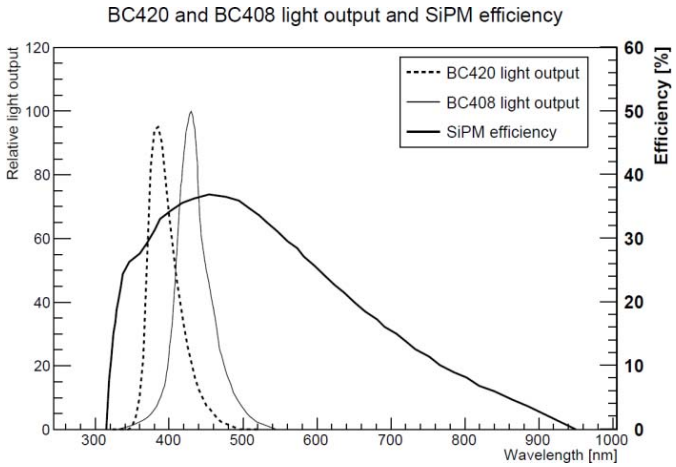

Fig. 6. Emission spectrum for BC-408 and BC-420 scintillators and MPPC S12472-025 photon detection efficiency plot.

planes along the beam axis. The maximum tracking rate is increased by dividing each plane into segments (called fingers) with the fingers of consecutive planes placed orthogonally to one another (Fig. 5). Each finger is composed of a fast plastic scintillator readout by a silicon photomultiplier (SiPM). To improve the range determination accuracy, the analog information from the SiPM of the fingers before the one where the proton comes at rest is also considered.

In the first stage of the project, two types of fast polyvinyl toluene plastic scintillators have been compared: BC-408 and BC-420, which, according to the datasheet, feature emission light decay times of 2.1 ns and 1.5 ns, respectively. The size of each single finger prototype was $200 \times 10 \times 5$ mm^3. First principle considerations and available literature data prompted us to start with 5 mm thick plastic scintillator planes, as thinner planes would not significantly increase the energy resolution, given the intrinsic proton range straggling of about 3–4 mm in our energy range [27].

Hamamatsu SiPM have been chosen for the iMPACT prototype development, due to their competitive technical features and the fact that they come in a ceramic mounting package which greatly helps system integration, a key benefit considering the great number of SiPM foreseen for the final calorimeter (about 2000). SiPM are available in different pitch: smaller pixel pitches are more suitable for applications where high photon fluxes are expected, while larger pixels guarantee a higher geometrical fill-factor, and an overall higher detection efficiency. Two different SiPM versions were at first considered: MPPC 1×1 mm^2, 15 μm cell (S12571-015C) and MPPC 3×3 mm^2, 25 μm cell (S12572-025C). Fig. 6 shows the emission spectra from the two scintillators and the photon detection efficiency of the MPPC S12572-025C SiPM. The SiPM efficiency matches both light output distributions of the scintillators considered, however, the BC-408 emission better fits the SiPM efficiency curve.

Monte Carlo simulations of the calorimeter have been developed both to optimize the detector constructive parameters and to generate experimental-like output data for testing the read-out chain and the data analysis software. The simulations were modeled using the GATE application, an advanced open source software dedicated to numerical simulations in medical imaging and radiotherapy [28], based on the Geant4 toolkit [29].

B. Light Yield

The calorimeter characterization started with an evaluation of the light collection efficiency. This depends both on the scintillator type and on the light gathering affected by several factors, including coating, size of the scintillating element, active surface of the SiPM, and SiPM quantum efficiency.

The light output from the scintillators BC-408 and BC-420 is about 10^4 photons per deposited MeV of energy [24], [25] (64% of light output of anthracene, which has a yield of $1.6 \cdot 10^4$ photons/MeV). From the proton linear energy transfer (LET), it is possible to estimate the light output per traveled distance through the scintillating calorimeter.

A 250 MeV proton, with an initial LET $\sim$ 0.5 MeV/mm (from SRIM simulations [26]) will produce about 2.5×10^4 photons in traversing a 5 mm thick scintillator. The proton loses energy as it penetrates inside the calorimeter. Near the end of range, at the Bragg peak, the LET is about six times larger as well as the expected number of photons.

Simulations and experimental tests show that a light gathering efficiency up to 10% (including the size of scintillator and of the S12572-025C SiPM, and the SiPM fill factor) can be achieved, even with direct SiPM/scintillator coupling (no tapering); a more conservative 5% value was adopted as baseline. We expect therefore approximately 1200 photons to reach the SiPM in the first calorimeter planes, and $\sim$7000 photons at the Bragg peak depth. Assuming a 25% detection efficiency at 380 nm (Fig. 6) then $\sim$300 photons are expected from the first scintillator planes and $\sim$1800 at the Bragg peak. This concerns the BC-420 scintillator, which has a light output peaked at $\sim$380 nm; the BC-408 scintillator features an emission spectrum with a peak ($\sim$ 430 nm) closer the maximum of the SiPM quantum efficiency, and would therefore provide a higher number of photons. The MPPC S12571-015C has ten times smaller area, causing the expected number of photons to drop further. The smaller surface SiPM would be faster, but the detection efficiency would be too low. The S12572-025C has been therefore chosen for all the following developments, in a compromise between speed and number of collected photons.

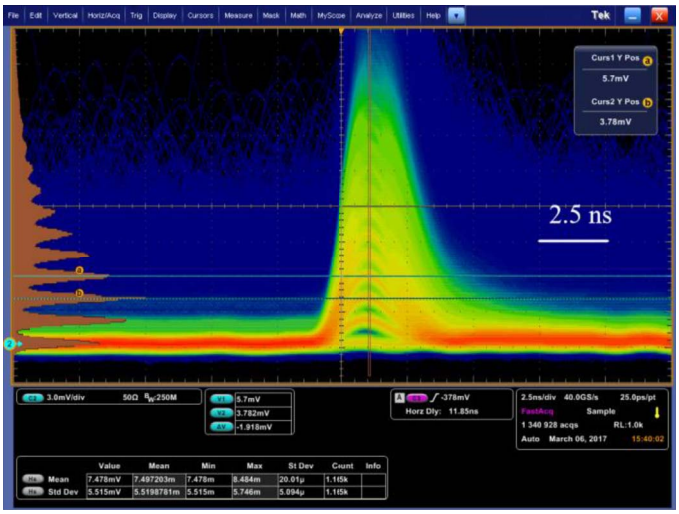

Fig. 7. Several few-photons overlying waveforms displayed on an oscilloscope screen-capture. The pulse height histogram is shown on the left of the screen, where the populations, due to different numbers of simultaneous photons, can be clearly distinguished. The time scale is 2.5 ns/div.

The scintillators, the SiPM and electronics were assembled (the SiPM was mounted on the smallest face of the scintillator using optical grease) in a preliminary experimental set-up. By using an ultrafast laser diode, together with a custom-made optical system to generate a controlled pulse of photons in a very short time interval (picoseconds), we characterized the SiPM readout response time for the different scintillators, SiPM types and electronic configurations (Fig. 7). We used this set-up to calibrate the systems and correlate the measured output signal amplitude to the number of detected photons.

To estimate the light yield and pulse shape generated by highly ionizing particles, tests were performed at the INFN Legnaro National Laboratories at the 7 MeV CN accelerator, using 3.5 and 5 MeV protons for the faster BC-420 scintillator. The scintillator-SiPM setup for this early test, housed in a vacuum chamber, was equipped with a fast, *ad-hoc* provisional read-out [the design of a dedicated electronics DAQ for the iMPACT calorimeter was still in progress (see Section V-C)].

Two different materials, Teflon and aluminum, were evaluated as possible choices for finger reflective wrapping. In both cases the opening of dedicated holes in the wrapping was necessary to allow such low energy protons enter the scintillator volume.

The results from the CN measurements confirmed the expected light yield (about 200 detected photons for 5 MeV protons, and 150 for 3.5 MeV), once we accounted for the immediate loss of 50% of the generated photons because of the particle entrance window in the scintillator wrapping, together with the point-like isotropic emission of photons along a few micrometer long path. In addition, these tests at the CN led us to discard aluminum due to a lower reflectivity respect to Teflon.

Nevertheless, the measurements also highlighted a nonexpected time structure of the light signal, where fast ripples are clearly visible at the output (Fig. 8). Detailed simulations with GATE were able to reproduce the effect, which is due to the high aspect ratio of the finger (20:1) and the statistical nature of the light signal formation in the scintillator, which becomes more apparent for low light yields.

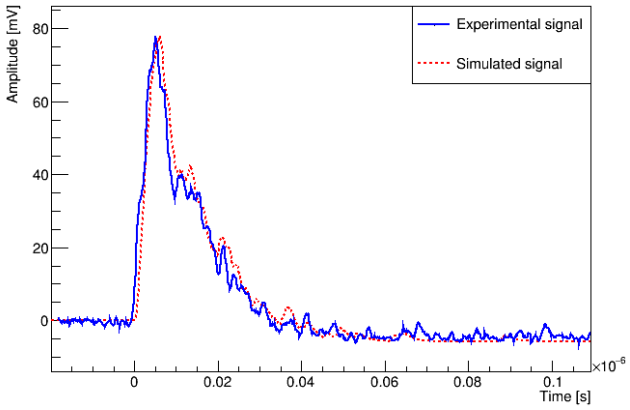

Fig. 8. Experimental (blue) and simulated (red) output signals from BC420 scintillator (5 MeV protons).

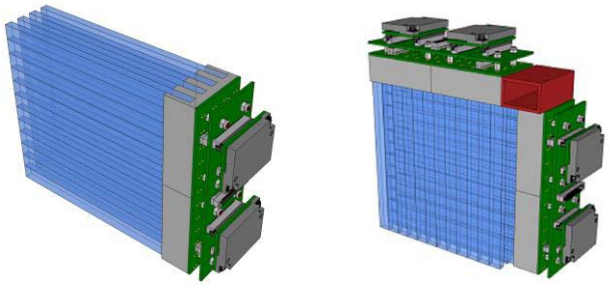

Fig. 9. Left: conceptual design of a module (8 × 4 sensors, one direction). Right: two modules (orthogonal directions) combined together to form a corner.

C. Electronics Development

For the design of the full calorimeter, we are following a modular approach, based on an array of 8 × 4 sensors, aligned in the same direction, with enough distance between planes to accommodate for a second identical module which can be interlayered to the first one to form a full "corner." The full calorimeter area can be covered by four such assembled corners. Stacking identical modules along the z-axis allows covering the full proton range.

Considering that a 250 MeV proton stops in ∼30 cm of Polyvinyl Toluene (the material of the plastic scintillators), at least 60 planes (5 mm thick) are necessary. Thousands of channels (2048 fingers in total for a configuration with 8 fingers per plane per corner, 4 corners, and 64 planes) will be therefore present in the final design. An analog readout at tens-hundreds of MHz of such a huge number of sensors is not practical and would be far too expensive for a commercial application. A digital readout is therefore considered, with a few threshold levels to keep some analog information.

We have developed a readout board for four channels (Fig. 10); each channel implements two analog stages for amplification and shaping, plus 4 comparators with programmable thresholds. An I^2C-controlled DAC generates independent, per channel programmable thresholds, to allow precise calibration of each SiPM-scintillator ensemble. SMA connectors are for debugging the analogue signal. This signal lasts 20 ns and shows a long undershoot; the baseline restores in about 100 ns. Two approaches are under investigation to eliminate the undershoot which at present limits the

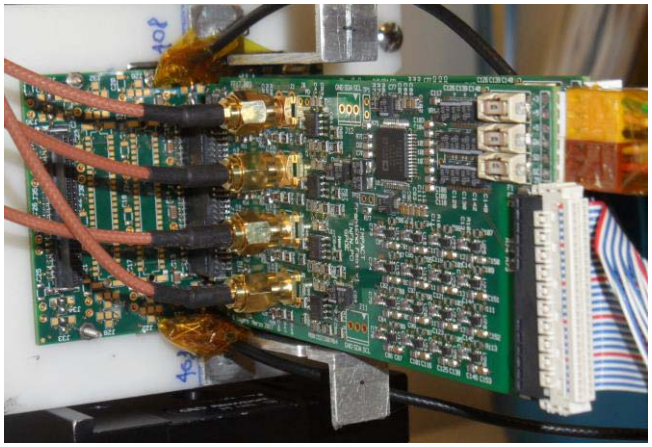

Fig. 10. Readout board for the iMPACT calorimeter.

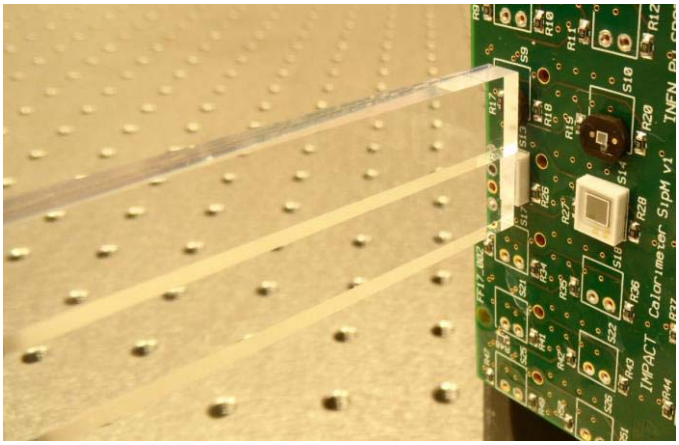

Fig. 11. Direct optical coupling of two 200 × 10 × 5 mm^3 scintillators to two different SiPM.

maximum achievable particle rate. Present prototypes show that a signal of the duration of 25 ns can be achieved, thus allowing for a particle rate higher than 4 MHz in the scintillator area (with a safety margin of a factor 10, to take into account the Poisson statistics). This version of the readout electronics was also designed to have a less steep rise with respect to the provisional one (i.e., the one used for the test beam of Fig. 8), in order to smooth the observed ripples. The bandwidths were 400 MHz and 1GHz, respectively. However, further cross-checks with cosmic rays on the two different scintillators types, readout by the two different electronics, have shown that the ripples in Fig. 8 were more related to the different type of scintillator, than on the readout electronics used.

Eight of these boards will be plugged onto another board hosting an 8 × 4 array of SiPMs (Fig. 11, with three empty slots on the left, and Fig. 12). This is the readout electronics of one single module.

The digital output from the fast comparators will be sent through LVDS lines to a field-programmable gate array (FPGA) module (TE0714-02-35-2IC6), which will collect data, perform zero suppression, pack the data and send them to the DAQ system, currently a National Instrument modular PXI system. The exact number and value of thresholds

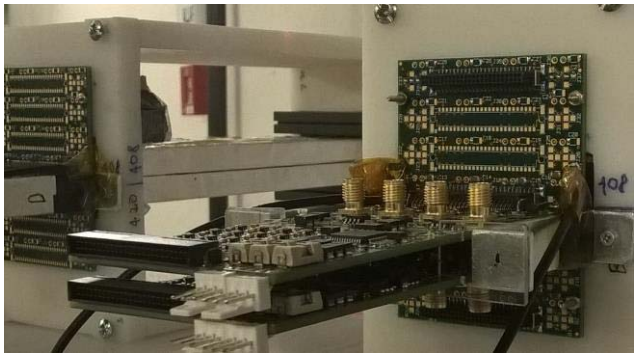

Fig. 12. Detail of the tested two-module arrangement: front-end electronics in front and scintillator fingers on the foreground/right. Numbers marking the scintillator type (BC-408 and BC-420) are visible.

are still to be optimized; two FPGA modules provide enough lines to manage up to 3 bits for each of the 32 channels of one calorimeter module.

We are in parallel investigating the possibility to use a fast frontend ASIC for the SiPM readout, which would make the system much more compact. The CITIROC 1A chip, produced by WEEROC [30], is presently under evaluation.

VI. Calorimeter Test

The front-end electronics described in the previous section has been used to characterize a mock-up of the final calorimeter in July 2017 at the TIFPA beam line hosted at the APSS Proton Therapy Centre (Trento, Italy), in conjunction with the test on the ALPIDE chip.

Two stations have been instrumented, with 8 fingers each, organized in two layers of 4 scintillators (Fig. 12) and wrapped with a Teflon layer and a protective aluminum foil, for a total aluminum thickness of about 800 μm. The entire top row included 8 identical BC-408 fingers and 3 mm × 3 mm Hamamatsu S12572-025c SiPM. The fingers arranged in the bottom row, instead, included six BC-420 coupled to two different SiPM models (four S12572-025C SiPM and two S12571-015C) and read-out electronics for comparison tests; two more BC-420 scintillators were mounted but no SiPM was available for readout. The analog channels were digitized with two PSI DRS4 boards [31].

The setup also included a Plexiglass absorber to mimic the missing calorimeter layers (Fig. 13).

The thickness of the absorber plus the 8 fingers was calibrated, using also results from simulation, to be about 28 cm, in order to stop 228 MeV protons. The relative position of the calorimeter modules and the absorber could be modified in order to measure the response to protons in different configurations. Each configuration has been tested with protons at 228, 70, and 35 MeV.

In particular, a configuration where all the eight scintillators were arranged in a row after the absorber was specifically studied to determine realistic values of the light output at the end of the plateau and at the Bragg Peak. The 8 waveforms from the different scintillator planes for a proton beam energy 228 MeV are shown in Fig. 14; signals are time-shifted for sake of clearness and follow quite well the expected profile

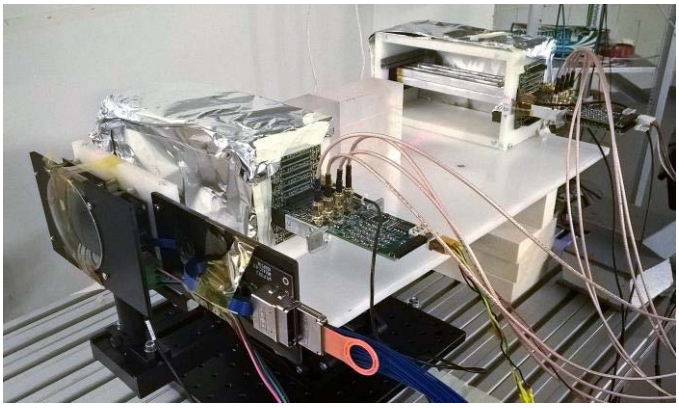

Fig. 13. Picture of the setup used at the APSS proton beamline. From the left: the ALPIDE chip independently tested, one calorimeter station, the beam absorber, and finally the second calorimeter station.

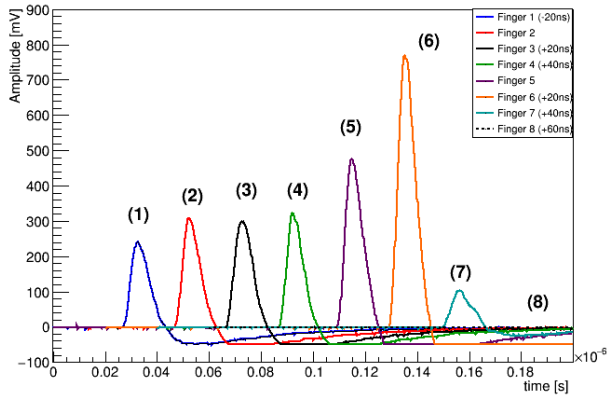

Fig. 14. Measured signals in the 8 fingers, from the same proton event.

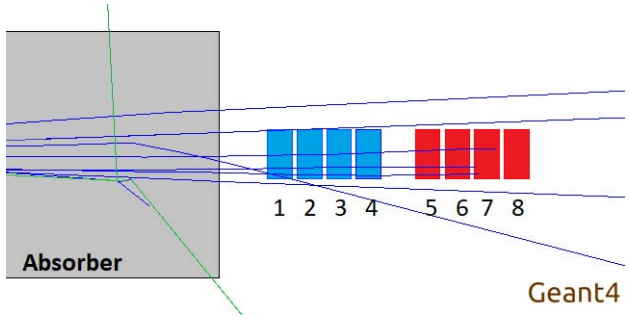

Fig. 15. Setup used for the test at the APSS proton beamline, as modeled in GATE, with superimposed proton tracks (blue). Neutrons (green), produced by nuclear reactions, are also visible.

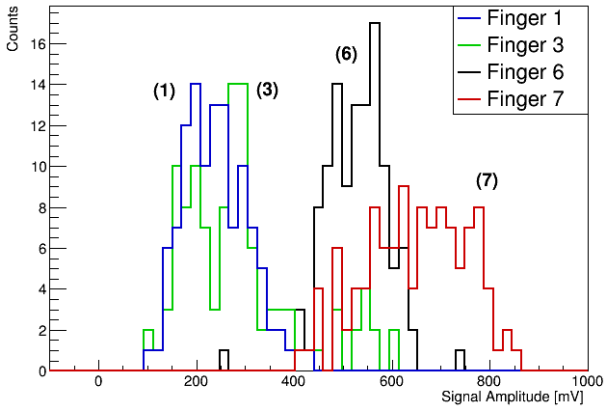

Fig. 16. Experimental signal amplitude spectrum from first (blue), third (green), sixth (black), and seventh (red) fingers, with threshold on $V_6 + V_7$.

of the Bragg curve. The amplitude of the first four layers is almost constant, corresponding to a proton in the plateau; the signals increase and reach the maximum (Bragg peak) around layer 6 (orange), then drops when the proton is about to stop in layer 7 (dark green); no signal is detected in layer 8, indicating that the proton has reached the end of its range.

The signal amplitudes in Fig. 14 indicate that the Bragg peak is located between the sixth and the seventh finger. The same picture, averaged over multiple protons (not presented herein), does not show an energy deposition profile as clear (i.e., the Bragg peak shape is broader) as the one obtained from a single proton event. This is due to a significant portion of the proton not releasing their entire residual energy inside the fingers. The fingers cover only 1 cm in the vertical direction, so protons passing through the first ones could deviate from a linear trajectory, enough to miss the following fingers. In order to clearly distinguish the Bragg peak and to build clear signal distributions of the different fingers, some cuts on the values on sixth and the seventh finger have to be applied. This setup was simulated with GATE (Fig. 15); combining experimental results and simulations data, a cut $V_6 + V_7 > 1100$ mV was chosen, since this efficiently selects protons stopping inside the fingers.

Experimental energy spectra from different fingers, with the threshold on $V_6 + V_7$ applied, are presented in Fig. 16. The first and the third finger spectra are, as expected, overlapped, being in the plateau region of the energy deposition profile. The seventh finger, where the highest average energy deposition takes place, shows a wider spectrum than the other ones, with a longer tail toward lower energies, which overlaps a portion of the sixth finger spectrum. The latter shows, instead, a narrower peak, distinguishable from the previous one. This clear separation between the finger in which the proton Bragg peak occurs, the previous one and those corresponding to the plateau region, indicates that a threshold-based digital discriminator for the iMPACT calorimeter read-out seems therefore feasible.

The simulated spectra from the first, third, sixth, and seventh fingers are shown in Fig. 17. The simulated spectra show a behavior comparable with the experimental ones: the spectra of the first fingers are similarly overlapped, as well as the seventh finger which presents a wider distribution and a lower energies tail. However, the sixth finger spectrum is shifted toward lower energies, and further from the seventh finger spectrum. In the experimental setup protons reach the last fingers with lower energies. The simulation, additionally, underestimates the energy distribution spread. The differences between the measurements and the simulations are likely due to the significant presence of additional materials in the experimental setup which were not included in the simulation: the ALPIDE sensor, along with the chip support and protective structures, the aluminum foil covering the scintillators, and the additional PVT fingers on top of the 8 BC-408. The presence of these materials cause a broadening of the beam dimensions, as well as a widening and lowering of the energy distribution.

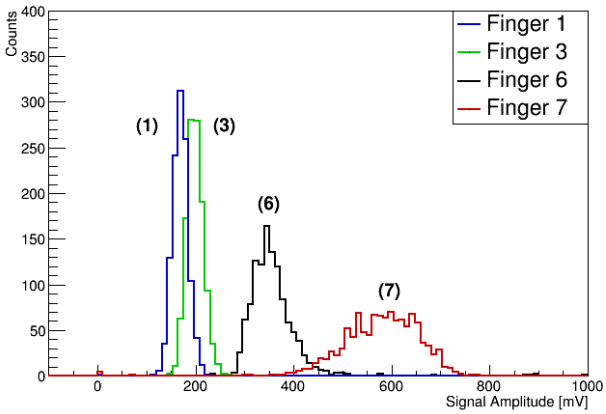

Fig. 17. Simulated signal amplitude spectrum from first (blue), third (green), sixth (black), and seventh (red) fingers, with threshold on $V_6 + V_7$.

Further discrepancies can derive from inaccurate modeling of the absorber dimension, chemical composition and density, as well as electronics noise. Simulation results were accurate enough for this prototyping phase, but need to be soon improved to provide more precise results.

VII. Conclusion

The building blocks of the iMPACT scanner have been developed and tested.

The first tests on the ALPIDE with protons in the 70–228 MeV energy range illustrate the potential of large area MAPS sensors in imaging applications.

The early prototype of the calorimeter has been extensively tested. The success of tests demonstrates that a full calorimeter is indeed feasible, and validates the idea of a hybrid energy-range calorimeter as an effective component of a fast and accurate proton tomography scanner.

A simulation tool has been also developed to study the behavior of the calorimeter and help choose among different design options. The simulation-based evaluations are qualitatively compatible with the actual measurements, for protons of different energy and impact position. The simulation code will be further optimized and will play a key role in guiding the full development of the iMPACT calorimeter.

References

[1] H. Suit *et al.*, "Proton vs carbon ion beams in the definitive radiation treatment of cancer patiens," *Radiother. Oncol.*, vol. 95, no. 1, pp. 3–22, 2010.

[2] A. Degiovanni and U. Amaldi, "History of hadron therapy accelerators," *Phys. Medica*, vol. 31, no. 4, pp. 322–332, 2015.

[3] H. F.-W. Sadrozinski *et al.*, "Toward proton computed tomography," *IEEE Trans. Nucl. Sci.*, vol. 51, no. 1, pp. 3–9, Feb. 2004.

[4] H. F.-W. Sadrozinski *et al.*, "Development of a head scanner for proton CT," *Nuclear Instrum. Methods A Accelerators Spectrometers Detectors Assoc. Equip.*, vol. 699, pp. 205–210, Jan. 2013.

[5] R. P. Johnson, "Review of medical radiography and tomography with proton beams," *Rep. Progress Phys.*, vol. 81, no. 1, 2018, Art. no. 016701.

[6] C. Civinini *et al.*, "Proton computed tomography: Iterative image reconstruction and dose evaluation," *J. Instrum.*, vol. 12, Jan. 2017, Art. no. C01034.

[7] V. Giacometti *et al.*, "Dosimetric evaluation of proton CT using a prototype proton CT scanner," in *Proc. Nuclear Sci. Symp. Med. Imag. Conf. Room Temp. Semicond. Detector Workshop (NSS/MIC/RTSD)*, 2016, pp. 1–3, doi: 10.1109/NSSMIC.2016.8069474.

[8] U. Schneider and E. Pedroni, "Multiple Coulomb scattering and spatial resolution in proton radiography," *Med. Phy.*, vol. 21, no. 11, pp. 1657–1663, 1994.

[9] D. C. Williams, "The most likely path of an energetic charged particle through a uniform medium," *Phys. Med. Biol.*, vol. 49, no. 13, pp. 2899–2911, 2002.

[10] H. Kasban, M. A. M. El-Bendary, and D. H. Salama, "A comparative study of medical imaging techniques," *Int. J. Inf. Sci. Intell. Syst.*, vol. 4, no. 2, pp. 37–58, 2015.

[11] M. Petterson *et al.*, "Proton radiography studies for proton CT," in *Proc. IEEE NSS-MIC Conf.*, San Diego, CA, USA, 2006, pp. 2276–2280.

[12] C. Civinini *et al.*, "Development of a proton computed tomography system for pre-clinical tests," in *Proc. IEEE Conf. NSS-MIC*, Anaheim, CA, USA, 2012, pp. 1279–1283.

[13] V. A. Bashkirov, R. P. Johnson, H. F.-W. Sadrozinski, and R. W. Schulte, "Development of proton computed tomography detectors for applications in hadron therapy," *Nuclear Instrum. Methods A Accelerators Spectrometers Detectors Assoc. Equip.*, vol. 809, pp. 120–129, Feb. 2016.

[14] S. A. Uzunyan *et al.*, "A new proton CT scanner," in *Proc. 23rd Conf. Appl. Accelerators Res. Ind. (CAARI)*, San Antonio, TX, USA, 2014.

[15] U. Amaldi *et al.*, "Construction, test and operation of a proton range radiography system," *Nuclear Instrum. Methods A Accelerators Spectrometers Detectors Assoc. Equip.*, vol. 629, no. 1, pp. 337–344, 2011.

[16] M. Bruzzi *et al.*, "Proton computed tomography images with algebraic reconstruction," *Nuclear Instrum. Methods A Accelerators Spectrometers Detectors Assoc. Equip.*, vol. 845, pp. 652–655, Feb. 2017.

[17] C. E. Ordoñez *et al.*, "A real-time image reconstruction system for particle treatment planning using proton computed tomography (pCT)," *Phys. Procedia*, vol. 90, pp. 193–199, Jul. 2017.

[18] S. Mattiazzo *et al.*, "Advanced proton imaging in computed tomography," *Radiat. Protect. Dosimetry*, vol. 166, nos. 1–4, pp. 388–392, 2015.

[19] S. Mattiazzo *et al.*, "The iMPACT project tracker and calorimeter," *Nucl. Instrum. Meth. A Accelerators Spectrometers Detectors Assoc. Equip.*, vol. 845, pp. 664–667, 2017.

[20] M. Oldhara *et al.*, "Progress of FD-SOI technology for monolithic pixel detectors," in *Proc. IEEE Conf. NSS-MIC*, Anaheim, CA, USA, 2012, pp. 471–474.

[21] G. A. Rinella, "The ALPIDE pixel sensor chip for the upgrade of the ALICE inner tracking system—On behalf of the ALICE collaboration," *Nuclear Instrum. Methods A Accelerators Spectrometers Detectors Assoc. Equip.*, vol. 845, pp. 583–587, Feb. 2017.

[22] F. Tommasino *et al.*, "Proton beam characterization in the experimental room of the Trento proton therapy facility," *Nuclear Instrum. Methods A Accelerators Spectrometers Detectors Assoc. Equip.*, vol. 869, pp. 15–20, Oct. 2017.

[23] A. Zatserklyaniy *et al.*, "A process modification for CMOS monolithic active pixel sensors for enhanced depletion, timing performance and radiation tolerance," *Nuclear Instrum. Methods A Accelerators Spectrometers Detectors Assoc. Equip.*, vol. 871, pp. 90–96, Nov. 2017.

[24] *BC-408 Premium Plastic Scintillators*. Accessed: May 8, 2018. [Online]. Available: https://www.crystals.saint-gobain.com/sites/imdf.crystals.com/files/documents/sgc-bc400-404-408-412-416-data-sheet.pdf

[25] *BC-420 Premium Plastic Scintillators*. Accessed: May 8, 2018. [Online]. Available: https://www.crystals.saint-gobain.com/sites/imdf.crystals.com/files/documents/sgc-bc418-420-422-data-sheet_69699.pdf

[26] SRIM. *The Stopping and Range of Ions in Matter*. Accessed: May 8, 2018. [Online]. Available: https://www.srim.org

[27] A. Zatserklyaniy *et al.*, "Development of a range Counter with SiPM readout for proton CT," in *Proc. Conf. IEEE NSS-MIC*, Anaheim, CA, USA, 2012, pp. 1326–1329.

[28] S. Jan *et al.*, "GATE: A simulation toolkit for PET and SPECT," *Phys. Med. Biol.*, vol. 49, no. 19, pp. 4543–4561, 2004.

[29] S. Agostinelli *et al.*, "Geant4—A simulation toolkit," *Nuclear Instrum. Methods A Accelerators Spectrometers Detectors Assoc. Equip.*, vol. 506, no. 3, pp. 250–303, 2003.

[30] *Citiroc 1A Documentation*. Accessed: May 8, 2018. [Online]. Available: http://www.weeroc.com/en/products/citiroc-1a

[31] *DRS4 Evaluation Board Documentation*. Accessed: May 8, 2018. [Online]. Available: https://www.psi.ch/drs/evaluation-board